



HAL
open science

A fumarole in a one-pot: synthesis, crystal structure and properties of Zn-and Mg-analogues of itelmenite and a synthetic analogue of glikinite

Diana O Nekrasova, Oleg I Siidra, Anatoly N Zaitsev, Valery Ugolkov, Marie Colmont, Dmitry Charkin, Olivier Mentré, Ruiqi Chen, Vadim M Kovrugin, Artem S Borisov

► To cite this version:

Diana O Nekrasova, Oleg I Siidra, Anatoly N Zaitsev, Valery Ugolkov, Marie Colmont, et al.. A fumarole in a one-pot: synthesis, crystal structure and properties of Zn-and Mg-analogues of itelmenite and a synthetic analogue of glikinite. *Physics and Chemistry of Minerals*, 2021, 48 (1), pp.6. 10.1007/s00269-020-01132-4 . hal-03438956v2

HAL Id: hal-03438956


<https://hal.science/hal-03438956v2>

Submitted on 24 Nov 2022

HAL is a multi-disciplinary open access archive for the deposit and dissemination of scientific research documents, whether they are published or not. The documents may come from teaching and research institutions in France or abroad, or from public or private research centers.

L'archive ouverte pluridisciplinaire **HAL**, est destinée au dépôt et à la diffusion de documents scientifiques de niveau recherche, publiés ou non, émanant des établissements d'enseignement et de recherche français ou étrangers, des laboratoires publics ou privés.

A fumarole in a one-pot: synthesis, crystal structure and properties of Zn- and Mg-analogs of itelmenite and a synthetic analog of glikinite

Diana O. Nekrasova^{1,2} · Oleg I. Siidra^{1,3}  · Anatoly N. Zaitsev⁴ · Valery L. Ugolkov³ · Marie Colmont² · Dmitry O. Charkin⁵ · Olivier Mentré² · Ruiqi Chen¹ · Vadim M. Kovrugin¹ · Artem S. Borisov¹

Received: 30 March 2020 / Accepted: 11 December 2020 / Published online: 11 January 2021
© The Author(s), under exclusive licence to Springer-Verlag GmbH, DE part of Springer Nature 2021

Abstract

Anhydrous sulfate minerals are abundant in the active fumaroles with highly oxidizing conditions on the scoria cones of the Tolbachik volcano. The mineral itelmenite, ideally $\text{Na}_2\text{CuMg}_2(\text{SO}_4)_4$, containing isomorphous admixture of Zn, was described in 2018, whereas glikinite, ideally $\text{Zn}_3\text{O}(\text{SO}_4)_2$, was described in 2020. Synthetic analogs of both minerals were obtained during studies of phase formation in the $\text{Na}_2\text{SO}_4\text{--CuSO}_4\text{--MgSO}_4\text{--}(\text{ZnSO}_4)$ systems which lead to essentially different results. Solid-state syntheses resulted in formation of several compounds previously known as minerals only. Both Zn- and Mg-containing analogs of itelmenite were prepared and exhibit slight deviations from the ideal $\text{Na}_2\text{CuM}_2(\text{SO}_4)_4$ stoichiometry. The Mg compound could be prepared single-phase which allowed the study of its thermal expansion and IR spectroscopy. $\text{Na}_2\text{CuMg}_2(\text{SO}_4)_4$ and $\text{Na}_2\text{CuZn}_2(\text{SO}_4)_4$ were evaluated for Na^+ -ion diffusion. For the Zn compound, several by-products were observed which are synthetic analogs of puninite $\text{Na}_2\text{Cu}_3\text{O}(\text{SO}_4)_2$, as well as hermannjahnite $\text{CuZn}(\text{SO}_4)_2$ and glikinite-type $(\text{Zn,Cu})_3\text{O}(\text{SO}_4)_2$. All of them were prepared via solid-state reactions in open systems. The $\text{Na}_2\text{CuMg}_2(\text{SO}_4)_4$, $\text{Na}_2\text{CuZn}_2(\text{SO}_4)_4$ and $(\text{Zn,Cu})_3\text{O}(\text{SO}_4)_2$ were structurally characterized by the single-crystal XRD. In the Zn-bearing system, the admixture of Cu^{2+} likely controls the formation of itelmenite-type and glikinite-type phases. The results of the experiments allowed to deduce possible scenarios of the formation processes of itelmenite and some other endemic fumarolic minerals. Our study shows that outstanding mineralogical diversity observed in the fumaroles of the Tolbachik scoria cones is not only due to the formation from the gas enriched by transition metals and involves also intensive exchange with the host basaltic scoria. Similar processes seem also to be responsible for the recrystallization of many other mineral species observed in high-temperature fumaroles resulted from the recent eruptions.

Keywords Anhydrous sulfates · Fumarolic mineral assemblages · MgSO_4 · ZnSO_4 · Solid-state reactions · Itelmenite · Glikinite · Hermannjahnite · Puninite · Framework structures · X-ray diffraction

Introduction

Minerals containing sulfate anions constitute one of the most diverse groups in terrestrial environments. About 400 species bearing SO_4^{2-} group are known to date. Most of the known sulfates are hydrates. A typical characteristic of

Supplementary Information The online version contains supplementary material available at <https://doi.org/10.1007/s00269-020-01132-4>.

anhydrous sulfates with alkali (and transition) metals is their high solubility.

Due to the fast-growing demands in new materials for various energy storage applications, various sulfate compounds have also been studied as promising electrode materials exhibiting relatively stable frameworks (their easy hydration remains a tremendous problem) and higher operating voltages (Barpanda 2015; Lander et al. 2018). Sulfates of sodium and some 3d-transition metals are extensively studied as promising materials for efficient Na-ion batteries. From structural viewpoint, the majority of these are synthetic analogs of known minerals. For example, sulfate of sodium and ferric iron, $\text{NaFe}(\text{SO}_4)_2$, was first discovered as a mineral eldfellite in 2009 (Balić Žunić et al. 2009) in a fumarole of Eldfell volcano, Iceland. Later (Singh et al. 2015), electrochemical properties were investigated on a full synthetic analog. A chemically related alluaudite-type sulfate of sodium and ferrous iron, $\text{Na}_2\text{Fe}_2(\text{SO}_4)_3$ (Barpanda et al. 2014) demonstrates outstanding electrochemical properties (3.8 V vs. Na^+/Na). A known disadvantage of minerals is the presence of impurities (due to both isomorphous substitution and by-phases), which does not allow detailed (and reproducible) studies of their physical properties.

There are but few geological environments on Earth where anhydrous alkali–transition metal sulfates can be found as mineral species: natural coal fires (e.g., Ravat, Tajikistan (Sharygin et al. 2009; Pautov et al. 2020)) and high-temperature volcanic fumaroles (Vergasova and Filatov 2012; Siidra et al. 2017). One of the largest numbers of active volcanoes is located at the Kamchatka Peninsula, Russia. The most interesting from a mineralogical point of view and relatively well studied are the fumaroles with highly oxidizing conditions on the scoria cones of the Tolbachik volcano (Pekov et al. 2018a). In the last century, eruptions on Tolbachik occurred in 1975–1976 (Fedotov and Markhinin, 1983); the most recently in 2012–2013 (Belousov et al. 2015). Of many new mineral species discovered in the past 30 years, the majority has no chemical and structural analogs reported among synthetic materials (Pekov et al. 2018b). The mineral itelmenite, ideally $\text{Na}_2\text{CuMg}_2(\text{SO}_4)_4$, containing isomorphous admixture of Zn, was described in 2018 (Nazarchuk et al. 2018); it was found in the fumarole on the Naboko scoria cone formed during the recent 2012–2013 eruption. Glikinite, ideally $\text{Zn}_3\text{O}(\text{SO}_4)_2$ (Nazarchuk et al. 2020), was collected from the sulfate zone of the arsenic-rich (or As-containing) Arsenatnaya fumarole on the Second scoria cone of the 1975–1976 eruption. Itelemente exhibits not only a new structure type, but also a new stoichiometry for anhydrous sulfates with alkali and transition metals: $A^+{}_2M^{2+}_3(\text{SO}_4)_4$. Glikinite has a synthetic structural analog (Bald and Grün 1981); however, the mineral (Nazarchuk et al. 2020) contains essential amount of copper

impurity. Synthetic analogs of both these mineral species were obtained in our studies of the $\text{Na}_2\text{SO}_4\text{--CuSO}_4\text{--MSO}_4$ ($M = \text{Mg, Zn}$) systems aimed at new possible materials for Na^+ -based batteries.

Despite the low conductive ability of the itelmenite-type $\text{Na}_2\text{CuM}_2(\text{SO}_4)_4$ framework, the results on phase formation in the $\text{Na}_2\text{SO}_4\text{--CuSO}_4\text{--MgSO}_4\text{--}(\text{ZnSO}_4)$ system appeared interesting with implications to mineralogy and geochemistry. Identified phases mimic fumarolic minerals assemblages, which allowed to deduce some of the secrets of the mineral formation in active fumaroles in scoria cones of Tolbachik volcano.

Synthesis

$\text{Na}_2\text{CuMg}_2(\text{SO}_4)_4$

Initially, a mixture of Na_2SO_4 (Alfa Aesar, 99%), CuSO_4 (Prolabo, 98%) and MgSO_4 (Alfa Aesar, 99%) reagents were taken in 1:1:2 ratio and were loaded into a platinum crucible and kept at 600 °C for 3 h in air and subsequently cooled for 9 h to room temperature. The product consisted of light-gray crystals and gray powder. Powder XRD analysis revealed the desired $\text{Na}_2\text{CuMg}_2(\text{SO}_4)_4$ and unreacted MgSO_4 . According to the starting stoichiometry, other (probably poorly crystallized) Na-containing products should also coexist. A single-phase specimen, ideally $\text{Na}_2\text{CuMg}_2(\text{SO}_4)_4$, was successfully synthesized only after the single-crystal XRD and the refinement of the crystal structure reported in detail below. Taking into account the refined occupancies of each site, we were able to prepare the pure product starting from Na_2SO_4 , CuSO_4 and MgSO_4 in 1:1.09:1.91 ratio. Taking in account the mixed occupancies of all *M* sites, one can expect a certain homogeneity range which was not investigated.

Thermal analysis (STA 429 CD NETZSCH) was performed to determine the crystallization temperatures of the Mg and Zn compounds. The powders (ca. 23 mg) were pressed into pellets (5.05 mm diameter and 0.7–0.8 mm height) using a steel die (pressure 1 kg/mm²). This technique, in comparison to using powdered samples, provides better reproducibility and precision of results. After weighing with precision of ± 10 µg, each pellet was loaded into a Pt–Rh crucible and mounted on a holder, after which TGA study was run at the heating rate of 20 °C/min in a dynamic atmosphere (air flow at 50 cm³/min) from 40 to 800–900 °C; cooling was performed down to 200 °C at the same rate. The gaseous decomposition products were analyzed on a QMS 403 C NETZSCH quadrupole mass spectrometer operating in a 1–121 *m/z* range.

Figure 1a represents TG, DSC, and IC (ionic currents at *m/z* = 18 and 48, which correspond to H_2O^+ and SO^+)

registered for a pelletized mixture of Na_2SO_4 , CuSO_4 , and MgSO_4 taken with the ratio described above upon heating from 40 to 850 °C and cooling to 720 °C.

The low-temperature part of TG curve exhibits two kinks due to mass loss: 1.33% at 56–95 °C, and 1.70% at 172–276 °C which are reflected as endothermic effects on the DSC curve with one maximum at 75 °C for the first one and two maxima at 214 and 241 °C for the second one, respectively. These are accompanied by the maxima for the $m/z = 18$ IC curve. Between the kinks, a monotonous mass loss of 1.04% is observed. The event at 214 °C may be related to partial melting of the sample.

These low-temperature effects clearly occur due to the dehydration processes. We note that the starting material rapidly absorbs water from humid air, most likely with formation of crystalline hydrates (Siidra et al. 2019), even when shortly exposed during opening the container and mounting onto the holder to the TGA apparatus. Note that water is an essential constituent of fumarolic gases (Chaplygin et al. 2016) therefore the experimental conditions still mimic the natural ones.

Further heating the sample proceeds eventlessly from 276 to 560 °C, after which a weak exothermic effect is observed with a maximum at 604 °C. At 617–653 °C, two endothermic effects are observed with maxima at 628 and 648 °C, which are accompanied by weight losses of 0.22%. We attribute a complicated series of effects to crystallization of $\text{Na}_2\text{CuMg}_2(\text{SO}_4)_4$. HT X-ray diffraction study of the reagent mixture (not represented herein) also confirms the appearance of itelmenite in this temperature range. Thus, the crystallization temperature of this compound is in a good agreement with the temperature of gases (600–620 °C) in Saranchinaitovaya fumarole where itelmenite was discovered in 2014 (Nazarchuk et al. 2018) yielding a good emulation of natural fumarolic processes.

The rate of mass loss increases essentially above 653 °C; further heating to 850 °C results in loss of 7.26% accompanied by a strong endothermic effect on the DSC curve (with a maximum at 767 °C and completion at 799 °C). The IC for $m/z = 48$ is observed only above 767 °C when the sample is almost completely melted. After that, the content of sulfur oxides in the decomposition products increases; this indicates that decomposition of sulfates occurs only after complete melting of the sample. It is reasonable to assume that the endothermic effect is due to the sample melting accompanied by the partial decomposition and evolution of sulfur oxides.

Cooling from 850 to 690 °C results in additional mass loss of 1.94%; the DSC curve shows a strong peak at 765 °C due to crystallization, after which evolution of sulfur oxides had stopped. It is possible that some decomposition products (e.g., polysulfuric acids) condense below 195 °C and do not enter the analyzing chamber of the mass spectrometer.

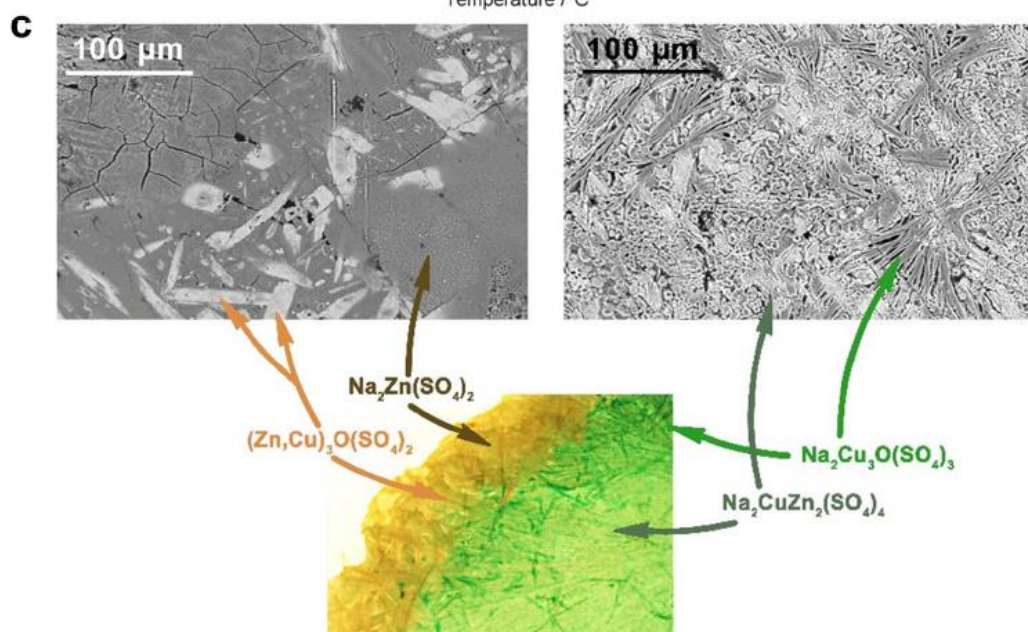
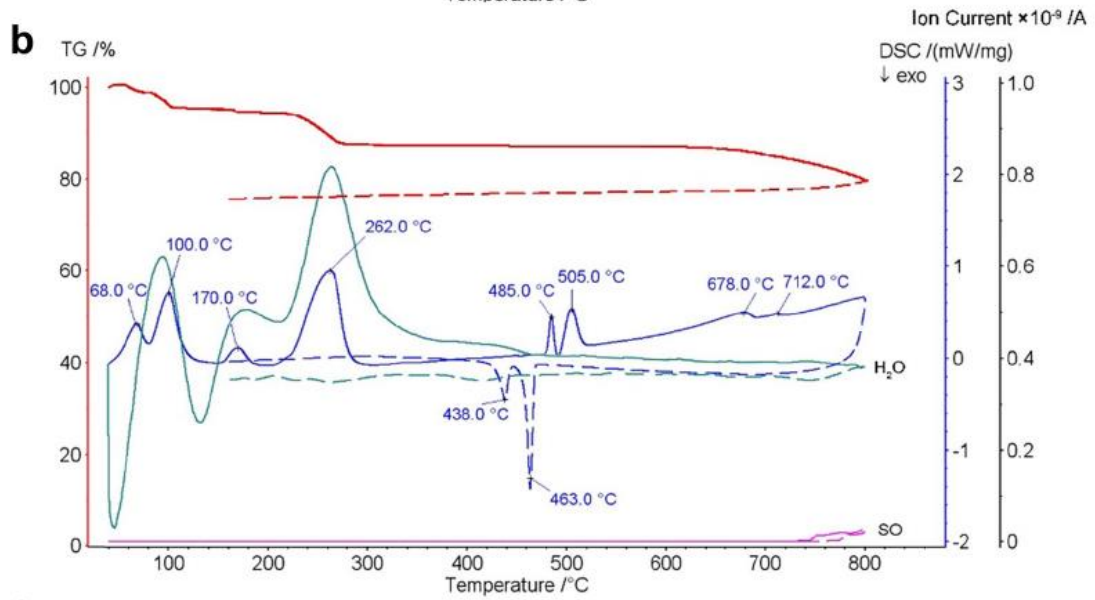
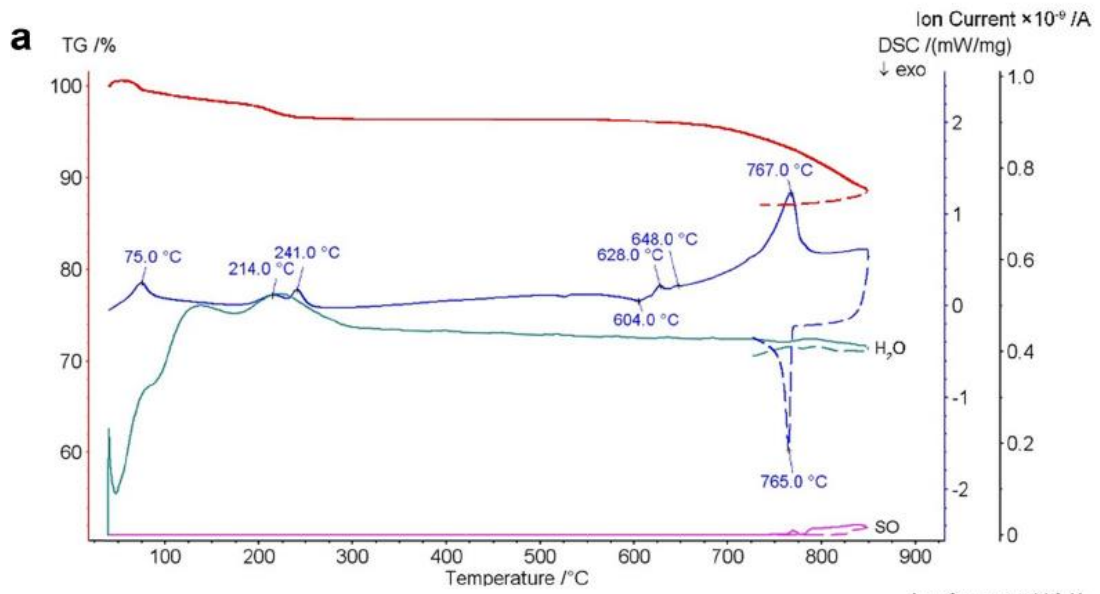
$\text{Na}_2\text{CuZn}_2(\text{SO}_4)_4$

We used the similar synthetic approach as described above for the Mg end-member compound: Na_2SO_4 (Alfa Aesar, 99%), CuSO_4 (Prolabo, 98%) and ZnSO_4 (Sigma-Aldrich, 99%) reagents were mixed in the “corrected” 1:1.09:1.91 ratio, as explained above. The mixture was loaded into a platinum crucible and kept at 500 °C (in accordance with thermal analysis data described below) for 1 h in air, followed by cooling for 9 h to room temperature. Visual inspection under an optical microscope revealed four crystalline phases different in color and morphology (Fig. 1c). Each of them was identified by the means of the single-crystal X-ray diffraction and SEM–EDX. Light-green crystalline matrix consisting of the irregularly shaped crystals (Fig. 1c) and formed on the bottom of the crucible was determined as the target $\text{Na}_2\text{CuZn}_2(\text{SO}_4)_4$. Unit-cell parameters of the grass-green prismatic crystals corresponded to the mineral puninite, $\text{Na}_2\text{Cu}_3\text{O}(\text{SO}_4)_3$ (Siidra et al. 2017). Closer to the crucible walls and upward, a well-crystallized zone of an orange-brown color (Fig. 1c) is observed. Unit-cell parameters of the two types of crystals in this zone correspond to recently discovered glikinite and synthetic $\text{Zn}_3\text{O}(\text{SO}_4)_2$ (Nazarchuk et al. 2020; Bald and Grünh 1981) and previously known synthetic $\text{Na}_2\text{Zn}(\text{SO}_4)_2$ (Berg and Thorup 2005). Different heating regimes were tried and none of them resulted in the single-phase sample of the $\text{Na}_2\text{CuZn}_2(\text{SO}_4)_4$. Crystal structure description and chemical compositions are reported below only for $\text{Na}_2\text{CuZn}_2(\text{SO}_4)_4$ and $(\text{Zn,Cu})_3\text{O}(\text{SO}_4)_2$.

Figure 1b shows the thermal analysis results for the pelletized mixture of Na_2SO_4 , CuSO_4 , and ZnSO_4 taken in the ratio listed above. The sample was heated from 40 to 800 °C and cooled to 150 °C at the same conditions as the previous one.

The initial heating stage is also accompanied by several essential thermal effects which are accompanied by maxima of the $m/z = 18$ ionic current, *i.e.*, they also correspond to release of absorbed water. Next essential endothermic effects are observed in the 477–526 °C range (corresponding maxima at 485 and 505 °C) accompanied by the mass loss of 0.05%. Crystallization of a multiphase sample (Fig. 1c), containing the desired $\text{Na}_2\text{CuZn}_2(\text{SO}_4)_4$, proceeds at essentially lower temperatures compared to its magnesium-based analog. This process is reflected by two very strong thermal effects. The 526–570 °C range is featureless, and monotonous mass loss is as low as 0.05%. No IC at $m/z = 48$ was observed.

An endothermic event starts at 583 °C, reaching its maximum at 678 °C and completing at 691 °C; the mass loss is 1.40%. This is rather common for decomposition processes, yet no peaks were observed on the IC curves. Most likely, the decomposition products had condensed before the analyzing chamber. Another endothermic process commences between



◀Fig. 1 TG-DSC-IC curves for the mixture of Na₂SO₄, CuSO₄ and MgSO₄ in 1:1.09:1.91 ratio (a), TG-DSC-IC curves for the mixture of Na₂SO₄, CuSO₄ and ZnSO₄ in 1:1.09:1.91 ratio (b). An image of the crucible bottom and wall covered by the various anhydrous sulfates obtained in Na₂SO₄-CuSO₄-ZnSO₄ system: grass-green needles of Na₂Cu₃O(SO₄)₃ (analog of puninite), light-orange needles of (Zn,Cu)₃O(SO₄)₂ (analog of glikinite), light-green polycrystalline matrix of Na₂CuZn₂(SO₄)₄ (Zn-analog of itelmenite) and light-brown matrix of Na₂Zn(SO₄)₂ (c). Two back-scattered electron microscope images of different colored zones are shown above: an orange-colored zone (orange arrows point on light prismatic and isometric crystals of (Zn,Cu)₃O(SO₄)₂; a dark-gray matrix consists of Na₂Zn(SO₄)₂ and marked by brown arrows) and green zone (sheaf-like dark-gray aggregates of Na₂Cu₃O(SO₄)₃ are marked by light-green arrows and dark-green arrows point on multiple irregularly shaped crystals of Na₂CuZn₂(SO₄)₄). Ideal formulas are given

691 and 718 °C with a maximum of 712 °C and mass loss of 0.98%. Further heating from 718 to 800 °C resulted in weight loss of 4.63%. No essential effects are observed on the DSC curve, while an ionic current at $m/z = 48$ was registered indicating release of sulfur oxides. It is possible that the decomposition mostly proceeded on the bottom of the Pt crucible.

Upon cooling, the DSC curve features two strong exothermal effects in the 471–417 °C (the corresponding maxima at 463 and 438 °C). These effects may indicate first-order transitions (most likely crystallization of several compounds formed upon heating). As in the previous case, weight loss continued upon cooling from 800 to 700 °C (2.23%).

Chemical composition

Two samples containing ideally Na₂CuZn₂(SO₄)₄ and (Zn,Cu)₃O(SO₄)₂ were mounted in epoxy resin and polished, to avoid degradation due to atmospheric moisture, without water and oil using a BUEHLER CarbiMet P1000, MicroCut P2500 and ChemoMet I. The samples have been studied using a Hitachi S-3400 N scanning electron microscope equipped with an Oxford Instruments X-Max 20 Energy-Dispersive Spectrometer and INCA Wave 500 wavelength dispersive spectrometer. The conditions for energy-dispersive analysis were: accelerating voltage 20 kV, electron beam current 1.0 nA and defocused electron beam

(up to 20 μm). The current was measured using a Faraday cup. X-ray acquisition time was 30 s and X-ray processing time '5' for analysis. System calibration was performed on CoK α -K β . X-ray matrix correction was carried-out automatically by the Oxford Instruments AZtecTru-Q including an exponential and pile-up correction routine.

The Na₂CuZn₂(SO₄)₄ compound contains 9.4–10.5 wt.% Na₂O, 25.7–29. wt.% ZnO, 9.2–12.8 wt.% CuO and 50.3–51.8 wt.% SO₃. Hence, the average composition of the phase (13 spot analyses, Table 1), calculated for $S = 4$, corresponds to Na_{2.03}Cu_{0.89}Zn_{2.10}(SO₄)₄ with variation of Zn between 2.00 and 2.24 atoms per formula unit (apfu) and Cu between 0.72 and 1.00 apfu. The general formula can be written as Na₂(Cu_{1-x}Zn_x)Zn₂(SO₄)₄ with $x = 0-0.24$.

The (Zn,Cu)₃O(SO₄)₂ phase, which occurs along with Na₂CuZn₂(SO₄)₄ (Fig. 2), is Na-free and contains 30.3–36.2 wt.% ZnO, 23.6–28.3 wt.% CuO and 39.4–41.4 wt.% SO₃. Its average composition (11 spot analyses, Table 1), calculated for $S = 2$, is (Zn_{1.68}Cu_{1.31})O(SO₄)₂ and general phase formula can be written as (Zn_{3-x}Cu_x)O(SO₄)₂, with $x = 1.20-1.45$.

In addition, the studied samples contain another Zn-Cu-S phase (ZnO = 26.3–27.6 wt.%, CuO = 21.3–22.6 wt.% and SO₃ = 49.1–49.7 wt.%, 5 spot analyses (Table 1)

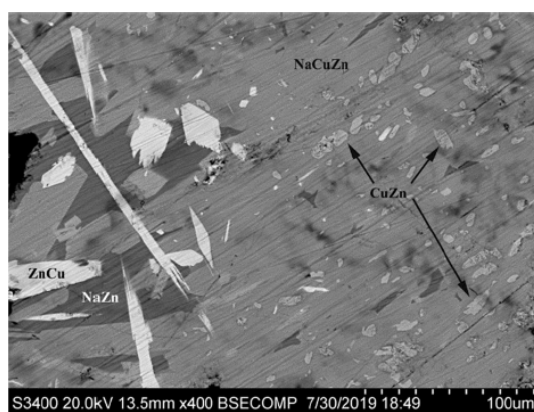


Fig. 2 Back-scattered electron image of the sample containing Na₂CuZn₂(SO₄)₄ (NaCuZn, gray), (Zn,Cu)₃O(SO₄)₂ (ZnCu, white), CuZn(SO₄)₂ (CuZn, light-gray) and Na₂Zn(SO₄)₂ (NaZn, dark-gray)

Table 1 Average compositions (wt. %) of Na₂CuZn₂(SO₄)₄, (Zn,Cu)₃O(SO₄)₂, CuZn(SO₄)₂ and Na₂Zn(SO₄)₂

Component	Na ₂ CuZn ₂ (SO ₄) ₄	(Zn,Cu) ₃ O(SO ₄) ₂	CuZn(SO ₄) ₂	Na ₂ Zn(SO ₄) ₂
Na ₂ O	10.01	bld	bld	19.07
ZnO	27.20	34.20	27.11	21.83
CuO	11.21	26.11	21.92	5.16
SO ₃	50.90	40.12	49.37	52.66
Total	99.32	100.43	98.40	98.72

bld - below detection limit

with average formula of $\text{Zn}_{1.08}\text{Cu}_{0.90}(\text{SO}_4)_2$ and a Na-Zn-Cu sulfate ($\text{Na}_2\text{O} = 18.5\text{--}20.0$ wt.%, $\text{ZnO} = 21.0\text{--}24.0$ wt.%, $\text{CuO} = 3.2\text{--}5.7$ wt.% and $\text{SO}_3 = 52.4\text{--}53.0$ wt.%, 6 spot analyses, Table 1) with average formula of $\text{Na}_{1.95}(\text{Zn}_{0.85}\text{Cu}_{0.20})(\text{SO}_4)_2$. Both phases were not studied using XRD or single-crystal analysis; the former probably corresponds to mineral hermannjahnite $\text{CuZn}(\text{SO}_4)_2$ (Siidra et al. 2018) and the latter has no analog among known minerals. $\text{Na}_2\text{Zn}(\text{SO}_4)_2$ (Berg and Thorup 2005) is known among synthetic compounds only.

Powder X-ray diffraction of $\text{Na}_2\text{CuMg}_2(\text{SO}_4)_4$

The X-ray powder diffraction pattern of $\text{Na}_2\text{CuMg}_2(\text{SO}_4)_4$ polycrystalline sample, obtained from Na_2SO_4 , CuSO_4 and MgSO_4 in 1:1.09:1.91 ratio, was collected at room temperature on a laboratory powder diffractometer (Rigaku Ultima IV, $\text{CuK}\alpha$ radiation). Data were collected with a step of 0.02° 2θ using a scanning speed of 3 s per step from 7° to 130° 2θ . The program JANA2006 (Petříček et al. 2014) was used to refine the crystal structure. The background was fitted using Chebyshev polynomial function, and the peak shapes were described by a Pseudo-Voigt function. The refined unit-cell parameters of $\text{Na}_2\text{CuMg}_2(\text{SO}_4)_4$ in *Pbca* space group are: $a = 9.5506(1)$ Å, $b = 8.7643(1)$ Å, $c = 28.7100(1)$ Å and $V = 2403.2(1)$ Å³, $R_p = 2.84\%$. The final observed, calculated, and difference powder XRD pattern resulting from the profile-matching procedure is plotted in Figure S1 which validates a single-phase sample.

Infrared spectroscopy of $\text{Na}_2\text{CuMg}_2(\text{SO}_4)_4$

In order to obtain infrared (IR) absorption spectra for the present study, powdered sample of $\text{Na}_2\text{CuMg}_2(\text{SO}_4)_4$, obtained from Na_2SO_4 , CuSO_4 and MgSO_4 in 1:1.09:1.91 ratio, was mixed with dried KBr, pelletized and analyzed from 4000 to 400 cm^{-1} using a Bruker Vertex 70 spectrometer (Bruker Optics) with a resolution of 4 cm^{-1} and 64 scans. The IR spectrum of an analogous pellet of pure KBr was used as a reference.

The IR spectrum of preliminary heat treated (to avoid hydration) $\text{Na}_2\text{CuMg}_2(\text{SO}_4)_4$ contains three groups of strong bands (in the ranges $464\text{--}496$, $605\text{--}674$ and $993\text{--}1277$ cm^{-1}) (Figure S2). Most of the observed peaks correspond to optically active modes of the three symmetrically independent SO_4 tetrahedra (Smith and Seshadri 1999). The peaks from 464 to 496 cm^{-1} can be tentatively assigned to Mg-O vibrations. The frequencies of the Cu-O stretching and O-Cu-O bending modes are out of the investigated region, i.e., $150\text{--}350$ cm^{-1} (Secco 1988).

Thermal analysis of $\text{Na}_2\text{CuMg}_2(\text{SO}_4)_4$

Thermal analysis of $\text{Na}_2\text{CuMg}_2(\text{SO}_4)_4$ was performed using a TGA 92-1600 SETARAM analyzer from room temperature to 650 °C (Figure S3). TGA curve demonstrates the stability up to 650 °C. However, one should note at ~ 50 °C a $7\text{--}8$ weight % loss, assigned to adsorbed H_2O , a systematic drawback dealing with sulfates.

High-temperature X-ray diffraction of $\text{Na}_2\text{CuMg}_2(\text{SO}_4)_4$

Thermal expansion of $\text{Na}_2\text{CuMg}_2(\text{SO}_4)_4$ was studied in air by means of a Rigaku Ultima X-ray diffractometer ($\text{CoK}\alpha$ radiation) with a high-temperature camera Rigaku HTA 1600. The sample was prepared from heptane's suspension on a Pt-Rh plate. The temperature step was 50 °C in the range $50\text{--}400$ °C and 20 °C in the range of $400\text{--}680$ °C. Unit-cell parameters at different temperatures were refined by least-square methods. Main coefficients of the thermal expansion tensor were determined using *ThetaToTensor* program (Firsova et al. 2011).

HTXRD data (Fig. 3a) are consistent with thermal analysis data reported above. In general, the pattern does not undergo significant changes. $\text{Na}_2\text{CuMg}_2(\text{SO}_4)_4$ starts to decompose at 620 °C and peaks of CuO start to appear. Using data up to the decomposition we found a volumetric dilatation coefficient $\alpha = 53 \cdot 10^{-6}$ °C which is rather high, in accordance with the rather "soft" framework offered by sulfates. However, this dilatation is strongly anisotropic, as verified plotting the temperature dependence of the cell parameters (Fig. 3b) of $\text{Na}_2\text{CuMg}_2(\text{SO}_4)_4$ in the appropriate thermal range. They can be expressed by the following functions after fitting, where the temperature T is expressed in °C:

$$a_t = 9.55759(59) + 0.1235(14) \times 10^{-3}T$$

$$b_t = 8.7675(10) + 0.0717(23) \times 10^{-3}T$$

$$c_t = 28.7345(86) + 0.330(58) \times 10^{-3}T + 0.885(84) \times 10^{-6}T^2$$

$$V_t = 2407.39(49) + 82(3) \times 10^{-3}T + 70(5) \times 10^{-6}T^2$$

It is noteworthy that the most expanding direction is the *c*-axis giving the first experimental clue about a rather anisotropic and complex structural framework, as detailed below.

with average formula of $\text{Zn}_{1.08}\text{Cu}_{0.90}(\text{SO}_4)_2$ and a Na-Zn-Cu sulfate ($\text{Na}_2\text{O} = 18.5\text{--}20.0$ wt.%, $\text{ZnO} = 21.0\text{--}24.0$ wt.%, $\text{CuO} = 3.2\text{--}5.7$ wt.% and $\text{SO}_3 = 52.4\text{--}53.0$ wt.%, 6 spot analyses, Table 1) with average formula of $\text{Na}_{1.95}(\text{Zn}_{0.85}\text{Cu}_{0.20})(\text{SO}_4)_2$. Both phases were not studied using XRD or single-crystal analysis; the former probably corresponds to mineral hermannjahnite $\text{CuZn}(\text{SO}_4)_2$ (Siidra et al. 2018) and the latter has no analog among known minerals. $\text{Na}_2\text{Zn}(\text{SO}_4)_2$ (Berg and Thorup 2005) is known among synthetic compounds only.

Powder X-ray diffraction of $\text{Na}_2\text{CuMg}_2(\text{SO}_4)_4$

The X-ray powder diffraction pattern of $\text{Na}_2\text{CuMg}_2(\text{SO}_4)_4$ polycrystalline sample, obtained from Na_2SO_4 , CuSO_4 and MgSO_4 in 1:1.09:1.91 ratio, was collected at room temperature on a laboratory powder diffractometer (Rigaku Ultima IV, $\text{CuK}\alpha$ radiation). Data were collected with a step of 0.02° 2θ using a scanning speed of 3 s per step from 7° to 130° 2θ . The program JANA2006 (Petříček et al. 2014) was used to refine the crystal structure. The background was fitted using Chebyshev polynomial function, and the peak shapes were described by a Pseudo-Voigt function. The refined unit-cell parameters of $\text{Na}_2\text{CuMg}_2(\text{SO}_4)_4$ in *Pbca* space group are: $a = 9.5506(1)$ Å, $b = 8.7643(1)$ Å, $c = 28.7100(1)$ Å and $V = 2403.2(1)$ Å³, $R_p = 2.84\%$. The final observed, calculated, and difference powder XRD pattern resulting from the profile-matching procedure is plotted in Figure S1 which validates a single-phase sample.

Infrared spectroscopy of $\text{Na}_2\text{CuMg}_2(\text{SO}_4)_4$

In order to obtain infrared (IR) absorption spectra for the present study, powdered sample of $\text{Na}_2\text{CuMg}_2(\text{SO}_4)_4$, obtained from Na_2SO_4 , CuSO_4 and MgSO_4 in 1:1.09:1.91 ratio, was mixed with dried KBr, pelletized and analyzed from 4000 to 400 cm^{-1} using a Bruker Vertex 70 spectrometer (Bruker Optics) with a resolution of 4 cm^{-1} and 64 scans. The IR spectrum of an analogous pellet of pure KBr was used as a reference.

The IR spectrum of preliminary heat treated (to avoid hydration) $\text{Na}_2\text{CuMg}_2(\text{SO}_4)_4$ contains three groups of strong bands (in the ranges $464\text{--}496$, $605\text{--}674$ and $993\text{--}1277$ cm^{-1}) (Figure S2). Most of the observed peaks correspond to optically active modes of the three symmetrically independent SO_4 tetrahedra (Smith and Seshadri 1999). The peaks from 464 to 496 cm^{-1} can be tentatively assigned to Mg-O vibrations. The frequencies of the Cu-O stretching and O-Cu-O bending modes are out of the investigated region, i.e., $150\text{--}350$ cm^{-1} (Secco 1988).

Thermal analysis of $\text{Na}_2\text{CuMg}_2(\text{SO}_4)_4$

Thermal analysis of $\text{Na}_2\text{CuMg}_2(\text{SO}_4)_4$ was performed using a TGA 92-1600 SETARAM analyzer from room temperature to 650 °C (Figure S3). TGA curve demonstrates the stability up to 650 °C. However, one should note at ~ 50 °C a $7\text{--}8$ weight % loss, assigned to adsorbed H_2O , a systematic drawback dealing with sulfates.

High-temperature X-ray diffraction of $\text{Na}_2\text{CuMg}_2(\text{SO}_4)_4$

Thermal expansion of $\text{Na}_2\text{CuMg}_2(\text{SO}_4)_4$ was studied in air by means of a Rigaku Ultima X-ray diffractometer ($\text{CoK}\alpha$ radiation) with a high-temperature camera Rigaku HTA 1600. The sample was prepared from heptane's suspension on a Pt-Rh plate. The temperature step was 50 °C in the range $50\text{--}400$ °C and 20 °C in the range of $400\text{--}680$ °C. Unit-cell parameters at different temperatures were refined by least-square methods. Main coefficients of the thermal expansion tensor were determined using *ThetaToTensor* program (Firsova et al. 2011).

HTXRD data (Fig. 3a) are consistent with thermal analysis data reported above. In general, the pattern does not undergo significant changes. $\text{Na}_2\text{CuMg}_2(\text{SO}_4)_4$ starts to decompose at 620 °C and peaks of CuO start to appear. Using data up to the decomposition we found a volumetric dilatation coefficient $\alpha = 53 \cdot 10^{-6}$ °C which is rather high, in accordance with the rather "soft" framework offered by sulfates. However, this dilation is strongly anisotropic, as verified plotting the temperature dependence of the cell parameters (Fig. 3b) of $\text{Na}_2\text{CuMg}_2(\text{SO}_4)_4$ in the appropriate thermal range. They can be expressed by the following functions after fitting, where the temperature T is expressed in °C:

$$a_t = 9.55759(59) + 0.1235(14) \times 10^{-3}T$$

$$b_t = 8.7675(10) + 0.0717(23) \times 10^{-3}T$$

$$c_t = 28.7345(86) + 0.330(58) \times 10^{-3}T + 0.885(84) \times 10^{-6}T^2$$

$$V_t = 2407.39(49) + 82(3) \times 10^{-3}T + 70(5) \times 10^{-6}T^2$$

It is noteworthy that the most expanding direction is the *c*-axis giving the first experimental clue about a rather anisotropic and complex structural framework, as detailed below.

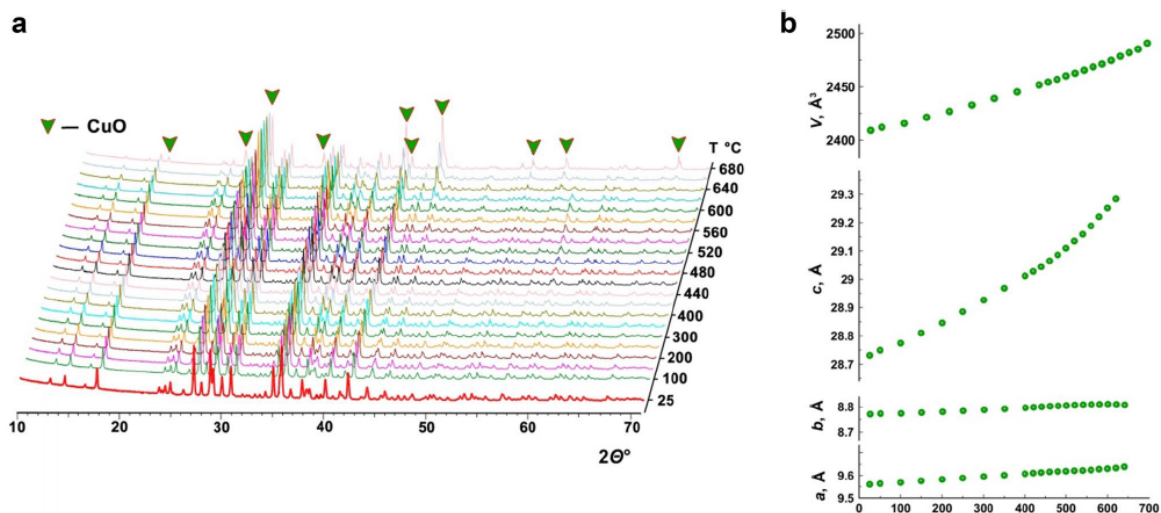


Fig. 3 Three-dimensional perspective plot showing all diffractograms for $\text{Na}_2\text{CuMg}_2(\text{SO}_4)_4$ over $10\text{--}75^\circ 2\theta$ with increasing temperature (a). The temperature dependences of the unit-cell parameters and volume for $\text{Na}_2\text{CuMg}_2(\text{SO}_4)_4$ (b)

Single-crystal X-ray diffraction analysis

Single crystals of $\text{Na}_2\text{CuMg}_2(\text{SO}_4)_4$, $\text{Na}_2\text{CuZn}_2(\text{SO}_4)_4$ and $(\text{Zn,Cu})_3\text{O}(\text{SO}_4)_2$ were mounted on thin glass fibers for X-ray diffraction analysis using Bruker APEX II DUO X-ray diffractometer with a microfocus X-ray tube operated with $\text{MoK}\alpha$ radiation at 50 kV and 0.6 mA. The data were integrated and corrected for absorption using a multiscan type model implemented in the Bruker program APEX2 (Bruker-AXS 2014). More than a hemisphere of X-ray diffraction data were collected for each crystal. Initial atomic coordinates for the crystal structures of $\text{Na}_2\text{CuMg}_2(\text{SO}_4)_4$ and $\text{Na}_2\text{CuZn}_2(\text{SO}_4)_4$ were taken from the structure of itelmenite (Nazarchuk et al. 2018). Both of the crystal structures were further refined in the $Pbca$ space group to $R_1=0.036$ and $R_1=0.053$ for $\text{Na}_2\text{CuMg}_2(\text{SO}_4)_4$ and $\text{Na}_2\text{CuZn}_2(\text{SO}_4)_4$, respectively using the SHELXL program (Sheldrick 2015). Atomic coordinates reported for glikinite (Nazarchuk et al. 2020) were refined to $R_1=0.053$ in the crystal structure of $(\text{Zn,Cu})_3\text{O}(\text{SO}_4)_2$. The main crystallographic information for all three new synthetic phases is summarized in Table 2. Selected interatomic distances are given in Tables 3 and 4.

Structure description

$\text{Na}_2\text{CuMg}_2(\text{SO}_4)_4$ and $\text{Na}_2\text{CuZn}_2(\text{SO}_4)_4$

There are three M sites (Fig. 4a), all coordinated by distorted octahedral arrays of O atoms with average $M\text{--O}$ distances in

the range, $2.08\text{--}2.17 \text{ \AA}$ (Table 3) in $\text{Na}_2\text{CuMg}_2(\text{SO}_4)_4$, $\text{Na}_2\text{CuZn}_2(\text{SO}_4)_4$ and itelmenite $\text{Na}_2\text{CuMg}_2(\text{SO}_4)_4$ (Nazarchuk et al., 2018). MO_6 polyhedron has five $M1\text{--O}$ bonds in the range $1.95\text{--}2.16 \text{ \AA}$ and sixth significantly longer $M1\text{--O}$ bond $\sim 2.8 \text{ \AA}$. Similar coordination environments are also observed for $M2$ site. Thus, both $M1$ and $M2$ can be described as Jahn–Teller-distorted MO_{5+1} coordinations. $M3$ site has symmetrical [6O] octahedral coordination with two slightly elongated apical bonds of $2.15\text{--}2.29 \text{ \AA}$. In general, substitution of Mg^{2+} ($r=0.72 \text{ \AA}$) by Zn^{2+} ($r=0.74 \text{ \AA}$) slightly increases $M\text{--O}$ bond lengths. MO_6 polyhedra are characterized by the different degree of distortion (Table 4). The following Δ_{oct} bond-length distortion parameter, suggested in Wildner 1992, was used for octahedrally coordinated M sites in both $\text{Na}_2\text{CuMg}_2(\text{SO}_4)_4$ and $\text{Na}_2\text{CuZn}_2(\text{SO}_4)_4$: $\Delta_{\text{oct}} = \frac{1}{6} \sum_{i=1}^6 \left[\frac{(d_i - d_m)}{d_m} \right]^2$ where $d_i = (M\text{--O})$ bond-length, $d_m = \langle M\text{--O} \rangle$ bond-length ($M = \text{Cu, Mg, Zn}$). All of the $M\text{--O}$ bonds $\leq 3 \text{ \AA}$ were taken into consideration (Table 3). Dealing with Mg^{2+} alkali earth against Cu^{2+} transition metal, the Δ_{oct} values correlate rather well with the content of Cu^{2+} cation in M sites due to the Cu^{2+} Jahn–Teller distortion. Cu:Mg ratio in M sites was obtained during the refinement of the crystal structure of $\text{Na}_2\text{CuMg}_2(\text{SO}_4)_4$ (Table 5). Cu^{2+} cation dominates in $M1$ site, whereas only 22.5% of copper is present in $M2$. The $M3$ site is almost completely occupied by Mg^{2+} cations in $\text{Na}_2\text{CuMg}_2(\text{SO}_4)_4$ in agreement with very symmetrical coordination environment.

Table 2 Crystallographic data for Na₂CuMg₂(SO₄)₄, Na₂CuZn₂(SO₄)₄ and (Zn,Cu)₃O(SO₄)₂

	Na ₂ CuMg ₂ (SO ₄) ₄	Na ₂ CuZn ₂ (SO ₄) ₄	(Zn,Cu) ₃ O(SO ₄) ₂
Crystal system	Orthorhombic	Orthorhombic	Monoclinic
Space group	<i>Pbca</i>	<i>Pbca</i>	<i>P2₁/m</i>
Unit-cell dimensions			
<i>a</i> (Å)	9.531 (7)	9.458 (5)	7.3156 (6)
<i>b</i> (Å)	8.745 (6)	8.811 (4)	6.6004 (5)
<i>c</i> (Å)	28.71 (2)	28.850 (15)	7.8941 (7)
β (°)			117.424 (5)
Unit-cell volume (Å ³)	2393 (3)	2404 (2)	338.34 (5)
Z	4	4	2
Calculated density (g•cm ⁻³)	3.032	3.450	3.968
Absorption coefficient (mm ⁻¹)	2.966	6.581	11.194
Crystal size (mm)	0.15×0.15×0.10	0.18×0.18×0.10	0.10×0.10×0.10
Data collection			
Temperature (K)	296(2)	296(2)	296(2)
Radiation, wavelength (Å)	MoK α , 0.71073	MoK α , 0.71073	MoK α , 0.71073
θ range (°)	1.418–26.757	1.412–27.997	2.907–27.466
<i>h, k, l</i> ranges	– 8 → 12 – 11 → 8 – 36 → 36	– 12 → 10 – 11 → 8 – 36 → 38	– 12 → 10 – 11 → 8 – 36 → 38
Total reflections collected	10,945	12,574	848
Unique reflections (<i>R</i> _{int})	2532 (0.06)	2894 (0.12)	844(0.02)
Unique reflections <i>F</i> > 4 σ (<i>F</i>)	1857	1679	783
Structure refinement			
Refinement method	Full-matrix least-squares on <i>F</i> ²	Full-matrix least-squares on <i>F</i> ²	Full-matrix least-squares on <i>F</i> ²
Weighting coefficients <i>a, b</i>	0.035000	0.048500	0.000200, 11.927700
Data/restraints/parameters	2532/0/230	2894/0/227	844/12/80
<i>R</i> ₁ [<i>F</i> > 4 σ (<i>F</i>)], <i>wR</i> ₂ [<i>F</i> > 4 σ (<i>F</i>)]	0.036, 0.074	0.053, 0.107	0.054, 0.104
<i>R</i> ₂ all, <i>wR</i> ₂ all	0.059, 0.083	0.113, 0.133	0.059, 0.107
Gof on <i>F</i> ²	1.006	0.958	1.144
Largest diff. peak and hole (e Å ⁻³)	0.538, – 0.487	1.104, – 0.941	1.747, – 1.698

The question of Cu²⁺ and Zn²⁺ cation distribution is significantly more difficult in Na₂CuZn₂(SO₄)₄, due to the very poor Cu/Zn scattering contrast by XRD. It can be only qualitatively (Table 5) partially answered on the basis of the different octahedral distortions of the Cu and Zn sites. Despite similar ionic radii, intuitively the Cu²⁺ Jahn–Teller effect is responsible for strong octahedral distortion. However, the second order Jahn–Teller effect which occurs for Zn²⁺ with a completely filled 3*d*¹⁰ shell (Boucher et al. 1994) can also lead to strong polyhedral distortion, such that Cu²⁺ for Zn²⁺ substitution in similar sites is possible. The strongest distortion is observed for M1O₅₊₁ octahedron in the crystal structures of both the mineral and its two synthetic analogs reported herein. The M3O₆ octahedron is obviously the least distorted preserving its main octahedral shape. Its

$\Delta_{\text{oct}} \times 10^3$ value is close to 1 for M3O₆ in itelmenite and synthetic Na₂CuMg₂(SO₄)₄. Importantly Δ_{oct} is preserved for M1O₅₊₁ and M2O₅₊₁ despite distance changes in the latter and significantly increased for M3O₆ in Na₂CuZn₂(SO₄)₄, where it is expected to be mostly occupied by Zn²⁺. According to these coordination changes after replacing Zn²⁺ for Mg²⁺, Cu²⁺ cations are expected dominant in M1 site in Na₂CuZn₂(SO₄)₄, and in minor amount in M2 and M3.

There are two positions fully occupied by Na in Na₂CuMg₂(SO₄)₄ and Na₂CuZn₂(SO₄)₄. Na1 atom forms ten Na–O bonds in the range 2.38–3.25 Å, whereas Na2 is coordinated by the eight O atoms in the range 2.38–2.87 Å. In the crystal structure of natural itelmenite (Nazarchuk et al. 2018), admixture of K is concentrated in Na1 site with the larger coordination sphere.

Table 3 Selected interatomic distances (in Å) in ietlmenite (Nazarchuk et al. 2018), Na₂CuMg₂(SO₄)₄ and Na₂CuZn₂(SO₄)₄

Ietlmenite		Na ₂ CuMg ₂ (SO ₄) ₄		Na ₂ CuZn ₂ (SO ₄) ₄	
M1-O14	1.961 (3)	Na2-O4	1.950 (3)	Na2-O4	2.376 (4)
M1-O13	1.961 (3)	Na2-O13	1.956 (3)	Na2-O13	2.448 (4)
M1-O16	1.976 (3)	Na2-O3	1.976 (3)	Na2-O3	2.459 (4)
M1-O2	2.032 (3)	Na2-O14	2.023 (3)	Na2-O14	2.462 (4)
M1-O3	2.153 (3)	Na2-O1	2.164 (3)	Na2-O7	2.530 (4)
M1-O2	2.826 (3)	Na2-O7	2.804 (3)	Na2-O1	2.533 (4)
<M1-O>	2.152	Na2-O10	2.146	Na2-O10	2.829 (4)
		Na2-O15	2.846 (3)	Na2-O15	2.830 (4)
M2-O11	1.980 (3)	<Na2-O>	1.962 (3)	<Na2-O>	2.558
M2-O8	2.028 (3)	M2-O11	2.005 (3)	M2-O8	2.021 (6)
M2-O9	2.048 (3)	M2-O9	2.026 (3)	M2-O9	2.026 (6)
M2-O6	2.050 (3)	SI-O15	1.445 (3)	SI-O15	1.443 (6)
M2-O5	2.168 (3)	SI-O8	1.457 (3)	SI-O8	1.454 (6)
M2-O12	2.791 (3)	SI-O12	1.475 (3)	SI-O12	1.465 (6)
<M2-O>	2.178	SI-O13	1.501 (3)	SI-O13	1.509 (6)
M3-O15	2.000 (3)	<SI-O>	1.470	<SI-O>	1.468
M3-O7	2.041 (3)	S2-O11	1.990 (3)	S2-O11	1.452 (6)
M3-O10	2.043 (3)	S2-O10	2.036 (3)	S2-O10	1.465 (6)
M3-O1	2.046 (3)	S2-O2	2.038 (3)	S2-O2	1.475 (6)
M3-O4	2.116 (3)	S2-O3	2.041 (3)	S2-O3	1.481 (5)
M3-O12	2.211 (3)	<S2-O>	2.127 (3)	<S2-O>	1.468
<M3-O>	2.076	S3-O7	2.222 (4)	S3-O4	1.469 (5)
		S3-O4	2.076	S3-O7	1.469 (6)
Na1-O3	2.393 (3)	S3-O1	2.375 (4)	S3-O1	1.480 (5)
Na1-O16	2.480 (4)	S3-O14	2.488 (4)	S3-O14	1.486 (6)
Na1-O5	2.493 (3)	<S3-O>	2.516 (4)	<S3-O>	1.476
Na1-O6	2.528 (3)	Na1-O6	2.525 (4)	Na1-O6	2.486 (7)
Na1-O13	2.725 (4)	Na1-O13	2.683 (4)	Na1-O13	2.686 (7)
Na1-O2	2.756 (3)	Na1-O2	2.728 (4)	Na1-O2	2.739 (7)
Na1-O8	2.876 (4)	Na1-O8	2.857 (4)	Na1-O8	2.743(7)
Na1-O9	2.879 (4)	Na1-O9	2.883 (4)	Na1-O9	2.888(7)
Na1-O16	3.134 (4)	Na1-O16	3.108 (4)	Na1-O16	3.142 (7)
Na1-O6	3.155 (4)	Na1-O6	3.175 (4)	Na1-O6	3.250 (7)
<Na1-O>	2.742	<Na1-O>	2.734	<Na1-O>	2.730

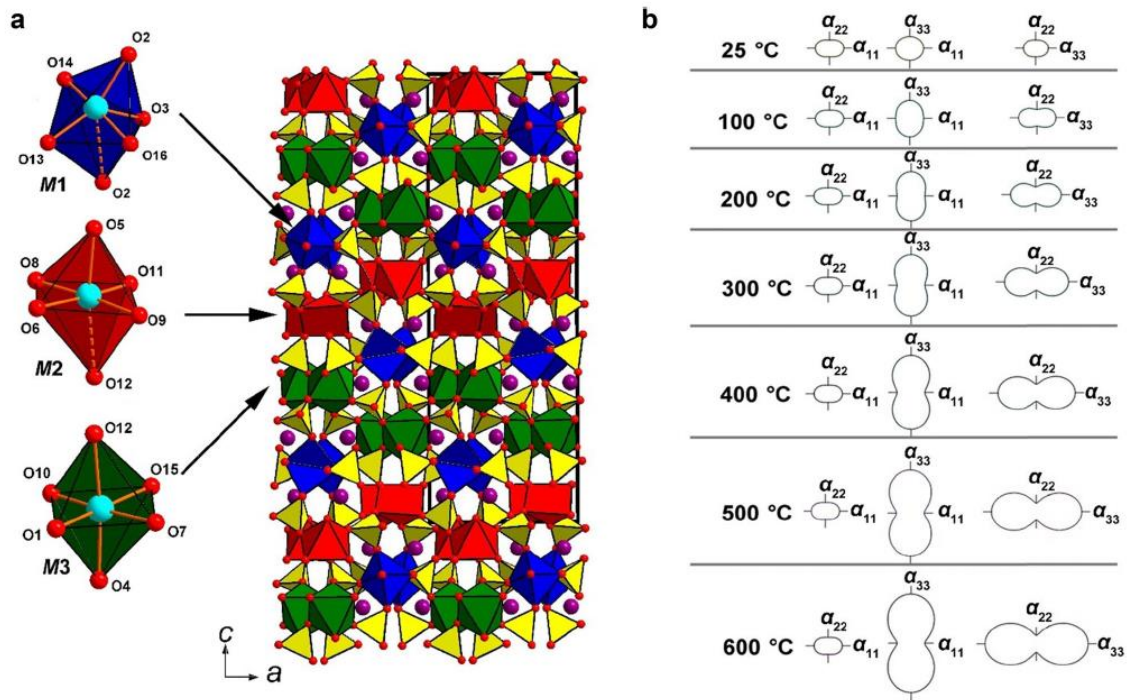


Fig. 4 Coordination of M sites in $\text{CuMg}_2\text{O}(\text{SO}_4)_2$ and $\text{CuZn}_2\text{O}(\text{SO}_4)_2$ (distances $< 2.5 \text{ \AA}$ are shown by dashed lines) (left) and general projection of the crystal structure of $\text{Na}_2\text{CuMg}_2(\text{SO}_4)_4$ along the b axis

(weak Cu–O bonds $> 2.5 \text{ \AA}$ are omitted for clarity) (a). Pole figures of the thermal expansion coefficients of $\text{Na}_2\text{CuMg}_2(\text{SO}_4)_4$ at different temperatures (b)

Table 4 Selected interatomic distances (in \AA) in glikinite (Nazarchuk et al. 2020) and $(\text{Zn,Cu})_3\text{O}(\text{SO}_4)_2$

Glikinite				$(\text{Zn,Cu})_3\text{O}(\text{SO}_4)_2$			
$M1-O1$	1.878 (5) $\times 2$	$S1-O7$	1.361 (15)	$M1-O1$	1.878 (4) $\times 2$	$S1-O7$	1.406 (18)
$M1-O2$	2.191 (10) $\times 2$	$S1-O6$	1.435 (18)	$M1-O2$	2.206 (9) $\times 2$	$S1-O6$	1.41 (2)
$M1-O4$	2.230 (10) $\times 2$	$S1-O4$	1.465 (13) $\times 2$	$M1-O4$	2.233 (10) $\times 2$	$S1-O4$	1.473 (10) $\times 2$
$\langle M1-O \rangle$	2.100	$\langle S1-O \rangle$	1.432	$\langle M1-O \rangle$	2.104	$\langle S1-O \rangle$	1.441
$M2-O6$	1.902 (17)	$S2-O5$	1.413 (14)	$M2-O6$	1.91 (2)	$S2-O5$	1.453 (11)
$M2-O1$	1.939 (12)	$S2-O3$	1.435 (13)	$M2-O3$	1.956 (12)	$S2-O3$	1.481 (12)
$M2-O3$	1.967 (14)	$S2-O2$	1.480 (12) $\times 2$	$M2-O1$	1.982 (13)	$S2-O2$	1.465 (10) $\times 2$
$M2-O2$	2.153 (13) $\times 2$	$\langle S2-O \rangle$	1.451	$M2-O2$	2.165 (10) $\times 2$	$\langle S2-O \rangle$	1.466
$\langle M2-O \rangle$	2.023			$\langle M2-O \rangle$	2.036		
		$O1-M1$	1.878 (5) $\times 2$			$O1-M1$	1.878 (4) $\times 2$
$M3-O7$	1.938 (15)	$O1-M2$	1.939 (12)	$M3-O7$	1.906 (19)	$O1-M2$	1.982 (13)
$M3-O5$	1.977 (14)	$O1-M3$	1.987 (13)	$M3-O1$	1.966 (13)	$O1-M3$	1.966 (13)
$M3-O1$	1.987 (13)	$\langle O1-M \rangle$	1.921	$M3-O5$	1.966 (12)	$\langle O1-M \rangle$	1.926
$M3-O4$	2.144 (15) $\times 2$			$M3-O4$	2.149 (11) $\times 2$		
$\langle M3-O \rangle$	2.038			$\langle M3-O \rangle$	2.027		

Four symmetrically independent S^{6+} cations show very similar S–O bond lengths in itelmenite and $\text{Na}_2\text{CuMg}_2(\text{SO}_4)_4$, $\text{Na}_2\text{CuZn}_2(\text{SO}_4)_4$. The $\langle \text{S–O} \rangle$ distances demonstrate very similar values of $\sim 1.47 \text{ \AA}$.

The structural architecture of $\text{Na}_2\text{CuMg}_2(\text{SO}_4)_4$ and $\text{Na}_2\text{CuZn}_2(\text{SO}_4)_4$ is simple, where each of the vertices of the SO_4 tetrahedron is common with one of the vertices of

Table 5 *M* site populations and $\Delta_{\text{oct}} \times 10^{-3}$ in the structures of itelmenite, $\text{Na}_2\text{CuMg}_2(\text{SO}_4)_4$ and $\text{Na}_2\text{CuZn}_2(\text{SO}_4)_4$

	Itelmenite (Nazarchuk et al. 2018)	$\Delta_{\text{oct}} \times 10^{-3}$	$\text{Na}_2\text{CuMg}_2(\text{SO}_4)_4$	$\Delta_{\text{oct}} \times 10^{-3}$	$\text{Na}_2\text{CuZn}_2(\text{SO}_4)_4$	$\Delta_{\text{oct}} \times 10^{-3}$
<i>M1</i>	$\text{Cu}_{0.71}\text{Mg}_{0.09}\text{Zn}_{0.2}$	20.62	$\text{Cu}_{0.820(5)}\text{Mg}_{0.180(5)}$	19.98	Cu > Zn	20.92
<i>M2</i>	$\text{Mg}_{0.55}\text{Cu}_{0.39}\text{Zn}_{0.06}$	16.55	$\text{Mg}_{0.775(4)}\text{Cu}_{0.225(4)}$	17.64	Zn > Cu	17.48
<i>M3</i>	$\text{Mg}_{0.91}\text{Zn}_{0.09}$	1.11	$\text{Mg}_{0.949(3)}\text{Cu}_{0.051(3)}$	1.38	Zn > Cu	2.18

the MO_6 octahedron. The resulting system of channels in the framework is filled by Na^+ cations (Fig. 4b). Itelmenite-type structural topology is unknown in synthetic compounds.

High-temperature powder X-ray diffraction studies (Fig. 3) show that $[\text{CuMg}_2(\text{SO}_4)_4]^{2-}$ framework upon heating expands anisotropically (Fig. 4b). Note that, at room temperature expansion is almost isotropic. The thermal expansion occurs mostly in the direction of α_{33} .

$(\text{Zn,Cu})_3\text{O}(\text{SO}_4)_2$

There are three *M* sites (Table 5) in the structure of synthetic analog of glikinite. Refinement of the crystal structure is complicated by the presence of the significant amount of Cu^{2+} (see chemical composition above) distributed over *M* sites. The *M1* site has a slightly distorted octahedral coordination with $\Delta_{\text{oct}} \times 10^{-3} = 5.87$. Relatively small value indicates only minor presence of Cu^{2+} in M1O_6 octahedron. *M2* and *M3* sites are 5-coordinated (Fig. 5a). Addison tau-parameter has been used to describe the distortion around *M2* and *M3* sites. Values of $\tau = 0.41$ and $\tau = 0.35$ for *M2* and *M3* sites, respectively, were calculated. Thus coordination

environments of both sites are intermediate from square pyramidal to trigonal bipyramidal geometry. M2O_5 and M3O_5 coordinations are more typical for Cu^{2+} rather than to Zn^{2+} . The question of the distribution of Cu^{2+} and Zn^{2+} in glikinite and its synthetic analog remains a debate.

Average S–O bond lengths show typical values of 1.441 and 1.466 Å for the S1O_4 and S2O_4 tetrahedra, respectively.

The structure of $(\text{Zn,Cu})_3\text{O}(\text{SO}_4)_2$ contains seven O^{2-} anions. The O2–O7 are strongly bonded in SO_4^{2-} groups. The O1 atom is tetrahedrally coordinated by four Zn^{2+} , Cu^{2+} cations, forming short and strong O–Zn bonds. From the viewpoint of bond valence theory, these bonds are the strongest in the structure and thus it makes absolute sense to consider the O1 atoms as centers of oxocentered $\text{O}(\text{Zn,Cu})_4$ tetrahedra. The mean O–Zn length in the O1Zn_4 tetrahedron is 1.926 Å, which is typical for such units (Krivovichev et al. 2013) taking into account high content of Cu^{2+} . The $\text{O}(\text{Zn,Cu})_4$ tetrahedra link together via common vertices to form $[(\text{Zn,Cu})_3\text{O}]^{4+}$ single chains (Fig. 5b). In this unit, each tetrahedron shares two of four vertices with adjacent tetrahedra. The $[(\text{Zn,Cu})_3\text{O}]^{4+}$ single chains extend along the *b*

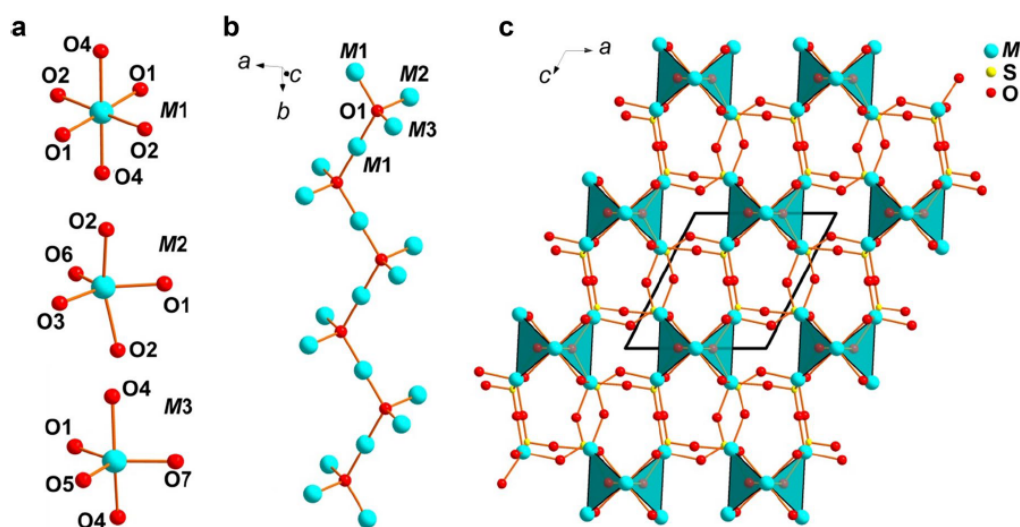


Fig. 5 Coordination of *M* sites in $(\text{Zn,Cu})_3\text{O}(\text{SO}_4)_2$ (a). $[\text{M}_3\text{O}]^{2+}$ chain elongated along the *b* axis (b). General projection of the crystal structure of $(\text{Zn,Cu})_3\text{O}(\text{SO}_4)_2$ (c). $[\text{M}_3\text{O}]^{2+}$ chains are highlighted by blue

axis. Oxocentered chains are interconnected via SO_4 groups into framework projected in Fig. 5c.

Evaluation of Na^+ -ion diffusion in $\text{Na}_2\text{CuM}_2(\text{SO}_4)_4$ ($M = \text{Mg}, \text{Zn}$)

The BVEL iso-energy surfaces were generated based on the structural data of the synthetic $\text{Na}_2\text{CuMg}_2(\text{SO}_4)_3$ phase using the BondStr program (FullProf Suite (Rodríguez-Carvajal, 1993)). Figure 6 demonstrates calculated possible Na^+ diffusion pathways in $\text{Na}_2\text{CuM}_2(\text{SO}_4)_4$ considering all counterions at distances up to 8 Å and the polarizability of Na^+ . An energy of 1.6 eV is usually considered as required percolation energy for the diffusion of Na^+ in conducting polyanionic compounds (Sun et al. 2015; Boivin et al. 2016; Kovrugin et al. 2018). In the framework of $\text{Na}_2\text{CuM}_2(\text{SO}_4)_4$, the iso-energy surface of 1.6 eV represents a non-interconnected ion diffusion path (Fig. 6a) indicating a limited Na^+ diffusion inside the structure. The energy level leading to an infinitely connected surface for Na^+ diffusion in $\text{Na}_2\text{CuM}_2(\text{SO}_4)_4$ corresponds only to 3.0 eV above the minimum energy level (Fig. 6b), which is a rather high energy barrier far above the expected BVEL calculations of $E_m < 1.5$ eV for any fast ion conductor (Katcho et al 2019) and, thus, the $\text{Na}_2\text{CuM}_2(\text{SO}_4)_4$ framework cannot be considered as a good Na^+ conductor. Meanwhile, it should be noted that a lithiated analog of the structure can probably induce a higher ionic conductivity (Boivin et al. 2017).

The estimated low conductivity of the $\text{Na}_2\text{CuM}_2(\text{SO}_4)_4$ framework is not surprising, since there is a number of works reporting a limited ion diffusion inside sulfate polyanionic structures (Lander et al. 2017; Kovrugin et al. 2019). However, we believe that the sulfate-based cathodes have a commercial potential in future considering the high

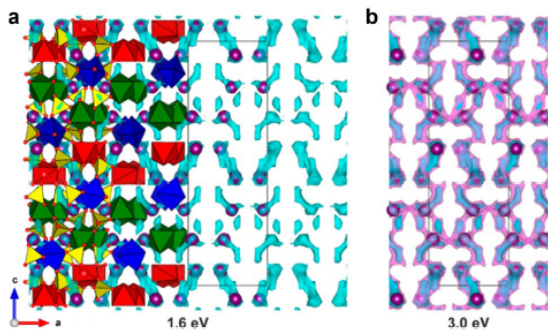


Fig. 6 Na^+ -ion diffusion pathways obtained using bond valence energy landscapes with an iso-energy surface value of 1.6 eV (a) and 3.0 eV (b) above the minimum energy level. The iso-energy surfaces of 1.6 and 3.0 eV are shown by cyan and pink, respectively. Legend for the unit-cell content see in Fig. 4

electronegative nature of sulfur, which may deliver the highest redox potential and lead to formation of cathode materials offering high voltage operation and, thus, competitive energy density overcoming weight penalties and lower theoretical capacity in comparison with conventional oxide cathodes.

Discussion

Our experiments indicate that investigation of anhydrous sulfate systems reproduces many compounds known before as mineral species only. It appeared possible to obtain the Zn- and Mg-analogs of itelmenite. Moreover, the latter was obtained as a pure phase which allowed the study of thermal expansion. The possibility of the formation of synthetic analogs of puninite $\text{Na}_2\text{Cu}_3\text{O}(\text{SO}_4)_2$ (Siidra et al. 2017), hermannjahnite $\text{CuZn}(\text{SO}_4)_2$ (Siidra et al. 2018) and glikinite $\text{Zn}_3\text{O}(\text{SO}_4)_2$ (Nazarchuk et al. 2020) as side products has been shown. On the other hand, the presence of $\text{Na}_2\text{Zn}(\text{SO}_4)_2$ compound (Berg and Thorup 2005) among the crystallized phases, unknown to date as a mineral, shows a high probability of finding such a mineral species in the fumaroles of the scoria cones of the Tolbachik volcano. Note that all the compounds synthesized in our work were obtained by the method of solid-state reactions in open air.

Earlier, in Nazarchuk et al. (2018), we have suggested that itelmenite may form as a result of the interaction between gas and basalt scoria. This hypothesis is confirmed by the syntheses and phase formation described above. Mg and possibly Na components in the fumarole come from the scoria, not from the gases. The concentrations of metals in the Tolbachik gases, during recent 2012–2013 eruption, are higher than the corresponding concentrations in high-temperature fumaroles worldwide (Zelenski et al. 2014). The hot Cu, Zn and sulfate bearing fumarolic gases condense on the surfaces of the scoria, forming a liquid which dissolves Na and Mg species from the basaltic scoria which then crystallize once the temperature is sufficiently low. Our study shows that outstanding mineralogical diversity observed in the fumaroles of scoria cones is not only due to the formation from the gas enriched by transition metals and involves also intensive exchange with the host basaltic scoria. The similar processes seem also to be responsible for the recrystallization of silicates described from deep and hot zones of Arsenatnaya fumarole (Shchipalkina et al. 2020).

The phase formation in the system with Mg turned out to be interesting and very different from the system with Zn. Apparently, such a difference can be explained by much lower melting point of ZnSO_4 (680 °C) compared with MgSO_4 (1137 °C). In addition, zinc has crystal chemical affinity for copper, which leads to a greater structural

diversity of the newly formed phases and more complex phase diagrams not available to date.

$\text{Zn}_3\text{O}(\text{SO}_4)_2$ phase was previously described by Bald and Grünh (1981). Interestingly, the polyhedra of zinc in the previously described Cu-free synthetic compound and the polyhedra with a significant admixture of copper in the $(\text{Zn,Cu})_3\text{O}(\text{SO}_4)_2$ described above and glikinite demonstrate very similar bond lengths and overall geometry. Jahn–Teller effect of Cu^{2+} in octahedral environment and the second order Jahn–Teller effect of Zn^{2+} result in distortions of similar magnitude (Halcrow 2013).

In our opinion, a significant amount of copper is important for the stabilization of this structure type and the formation of oxocentered $[(\text{Zn,Cu})_3\text{O}]^{4+}$ units. Admixture of Cu^{2+} also controls the formation of itelmenite-type phases.

Acknowledgements We are grateful to Tonči Balić-Žunić, Wulf Depmeier and an anonymous reviewer for valuable comments. This work was financially supported by the Russian Science Foundation through the grant 16-17-10085. Technical support by the SPbSU X-ray Diffraction and Geomodel Resource Centers is gratefully acknowledged. The Chevreul Institute (FR 2638), the Ministère de l'Enseignement Supérieur et de la Recherche, the Région Hauts-de-France, the CNRS, and the FEDER are acknowledged for supporting and funding this work.

References

- Bald L, Grünh R (1981) Die Kristallstruktur von einem Sulfat-reichen Oxidsulfat des Zinks. *Naturwissenschaften* 68:39–39
- Balić Žunić T, Garavelli A, Acquafredda P, Leonardsen E, Jakobsson SP (2009) Eldfellite, a new fumarolic mineral from Eldfell volcano, Iceland. *Mineral Mag* 73:51–57
- Barpanda P (2015) Sulfate chemistry for high-voltage insertion materials: synthetic, structural and electrochemical insights. *Isr J Chem* 55:537–557
- Barpanda P, Oyama G, Nishimura S, Chung S-C, Yamada A (2014) A 3.8-V earth-abundant sodium battery electrode. *Nat Commun* 5:4358
- Belousova A, Belousova M, Edwards B, Volynets A, Melnikov D (2015) Overview of the precursors and dynamics of the 2012–13 basaltic fissure eruption of Tolbachik Volcano, Kamchatka, Russia. *J Volcanol Geoth Res* 307:22–37
- Berg RW, Thorup N (2005) The reaction between ZnO and molten $\text{Na}_2\text{S}_2\text{O}_7$ or $\text{K}_2\text{S}_2\text{O}_7$ forming $\text{Na}_2\text{Zn}(\text{SO}_4)_2$ or $\text{K}_2\text{Zn}(\text{SO}_4)_2$, studied by Raman spectroscopy and X-ray diffraction. *Inorg Chem* 44:3485–3493
- Boivin E, Chotard J-N, Ménétrier M, Bourgeois L, Bamine T, Carlier D, Fauth F, Suard E, Masquelier C, Croguennec L (2016) Structural and electrochemical studies of a new Tavorite composition: LiVPO_4OH . *J Mater Chem A* 4:11030–11045
- Boivin E, Chotard J-N, Bamine T, Carlier D, Serras P, Palomares V, Rojo T, Iadecola A, Dupont L, Bourgeois L, Fauth F, Masquelier C, Croguennec L (2017) Vanadyl-type defects in Tavorite-like NaVPO_4F : from the average long range structure to local environments. *J Mater Chem A* 5:25044–25055
- Boucher F, Evain M, Brec R (1994) Second-order Jahn-Teller effect in CdPS_3 and ZnPS_3 demonstrated by a non-harmonic behaviour of Cd^{2+} and Zn^{2+} d^{10} ions. *J Alloy Compd* 215:63–70
- Bruker-AXS (2014) APEX2. Version 2014.11–0. Madison, Wisconsin, USA
- Chaplygin I, Lavrushin V, Dubinina E, Bychkova YV, Inguaggiato S, Yudovskaya M (2016) Geochemistry of volcanic gas at the 2012–13 New Tolbachik eruption, Kamchatka. *J Volcanol Geoth Res* 323:186–193
- Fedotov SA, Markhinin YK (eds) (1983) The Great Tolbachik Fissure Eruption. Cambridge Univ. Press, New York
- Firsova VA, Bubnova RS, Filatov SK (2011) Program for the thermal expansion tensor determination for crystalline materials. Institute of Silicate Chemistry of Russ. Acad. Sci, St. Petersburg, Russia
- Halcrow MA (2013) Jahn-Teller distortions in transition metal compounds, and their importance in functional molecular and inorganic materials. *Chem Soc Rev* 42:1784–1795
- Katcho NA, Carrete J, Reynaud M, Rouse G, Casas-Cabanas M, Mingo N, Rodríguez-Carvajal J, Carrasco J (2019) An investigation of the structural properties of Li and Na fast ion conductors using high-throughput bond-valence calculations and machine learning. *J Appl Cryst* 52:148–157
- Kovrugin VM, David R, Chotard J-N, Recham N, Masquelier C (2018) A high voltage cathode material for sodium batteries: $\text{Na}_3\text{V}(\text{PO}_4)_2$. *Inorg Chem* 57:8760–8768
- Kovrugin VM, Nekrasova DO, Siidra OI, Mentré O, Masquelier C, Stefanovich SY, Colmont M (2019) Mineral-inspired crystal growth and physical properties of $\text{Na}_2\text{Cu}(\text{SO}_4)_2$ and review of $\text{Na}_2\text{M}(\text{SO}_4)_2(\text{H}_2\text{O})_x$ ($x = 0–6$) compounds. *Cryst Growth Des* 19:1233–1244
- Krivovichev SV, Mentré O, Siidra OI, Colmont M, Filatov SK (2013) Anion-centered tetrahedra in inorganic compounds. *Chem Rev* 113:6459–6535
- Lander L, Rouse G, Batuk D, Colin CV, Dalla Corte DA, Tarascon J-M (2017) Synthesis, structure, and electrochemical properties of K-based sulfates $\text{K}_2\text{M}_2(\text{SO}_4)_3$ with $\text{M} = \text{Fe}$ and Cu . *Inorg Chem* 56:2013–2021
- Lander L, Tarascon J-M, Yamada A (2018) Sulfate-based cathode materials for Li- and Na-ion batteries. *Chem Rec* 18:1394–1408
- Nazarchuk EV, Siidra OI, Agakhanov AA, Lukina EA, Avdontseva EY, Karpov GA (2018) Itelmenite, $\text{Na}_2\text{CuMg}_2(\text{SO}_4)_4$, a new anhydrous sulphate mineral from the Tolbachik volcano. *Mineral Mag* 82:1233–1241
- Nazarchuk EV, Siidra OI, Nekrasova DO, Shilovskikh VV, Borisov AS, Avdontseva EYu (2020) Glikinite, $\text{Zn}_3\text{O}(\text{SO}_4)_2$, a new anhydrous zinc oxysulphate mineral structurally based on OZn_4 tetrahedra. *Mineral Mag* 84:563–567
- Pautov LA, Mirakov MA, Siidra OI, Faiziev AR, Nazarchuk EV, Karpenko VYu, Makhmadsharif S (2020) Falgarite, $\text{K}_4(\text{VO})_3(\text{SO}_4)_5$, a new mineral from sublimates of a natural underground coal fire at the tract of Kukhi-Malik, Fan-Yagnob coal deposit, Tajikistan. *Mineral Mag* 84:455–462
- Pekov IV, Koshlyakova NN, Zubkova NV, Lykova IS, Britvin SN, Yapaskurt VO, Agakhanov AA, Shchepalkina NV, Turchkova AG, Sidorov EG (2018a) Fumarolic arsenates - a special type of arsenic mineralization. *Eur J Mineral* 30:305–322
- Pekov IV, Zubkova NV, Pushcharovsky DYu (2018b) Copper minerals from volcanic exhalations—a unique family of natural compounds: crystal-chemical review. *Acta Crystallogr B* 74:502–518
- Petříček V, Dušek M, Palatinus L (2014) Crystallographic computing system JANA2006: general features. *Z Kristallogr Cryst Mater* 229:345–352
- Rodríguez-Carvajal J (1993) Recent advances in magnetic structure determination by neutron powder diffraction. *Phys B* 192:55–69
- Secco EA (1988) Spectroscopic properties of SO_4 (and OH) in different molecular and crystalline environments. I. Infrared spectra of $\text{Cu}_4(\text{OH})_6\text{SO}_4$, $\text{Cu}_4(\text{OH})_4\text{OSO}_4$, and $\text{Cu}_3(\text{OH})_4\text{SO}_4$. *Can J Chem* 66:329–336

- Sharygin VV, Sokol EV, Belakovski DI (2009) Fayalite-sekaninaite paralava from the Ravat coal fire (central Tajikistan). *Russ Geol Geophys* 50:703–721
- Shchipalkina NV, Pekov IV, Koshlyakova NN, Britvin SN, Zubkova NV, Varlamov DA, Sidorov EG (2020) Unusual silicate mineralization in fumarolic sublimates of the Tolbachik volcano, Kamchatka, Russia—Part 1: Neso-, cyclo-, ino- and phyllosilicates. *Eur J Mineral* 32:101–119
- Sheldrick GM (2015) Crystal structure refinement with SHELXL. *Acta Crystallogr C* 71:3–8
- Siidra OI, Nazarchuk EV, Zaitsev AN, Lukina EA, Avdontseva EY, Vergasova LP, Vlasenko NS, Filatov SK, Turner R, Karpov GA (2017) Copper oxosulphates from fumaroles of Tolbachik Volcano: puninite, $\text{Na}_2\text{Cu}_3\text{O}(\text{SO}_4)_3$ —a new mineral species and structure refinements of kamchatkite and alumoklyuchevskite. *Eur J Mineral* 29:499–510
- Siidra OI, Nazarchuk EV, Agakhanov AA, Lukina EA, Zaitsev AN, Turner R, Filatov SK, Pekov IV, Karpov GA, Yapaskurt VO (2018) Hermannjahnite, $\text{CuZn}(\text{SO}_4)_2$, a new mineral with chalcocyanite derivative structure from the Naboko scoria cone of the 2012–2013 fissure eruption at Tolbachik volcano, Kamchatka, Russia. *Miner Petrol* 112:123–134
- Siidra OI, Borisov AS, Lukina EA, Depmeier W, Platonova NV, Colmont M, Nekrasova DO (2019) Reversible hydration/dehydration and thermal expansion of euchlorine, ideally $\text{KNaCu}_3\text{O}(\text{SO}_4)_3$. *Phys Chem Miner* 46:403–416
- Singh P, Shiva K, Celio H, Goodenough JB (2015) Eldfellite, $\text{NaFe}(\text{SO}_4)_2$: an intercalation cathode host for low-cost Na-ion batteries. *Energ Environ Sci* 8:3000–3005
- Smith DH, Seshadri KS (1999) Infrared spectra of $\text{Mg}_2\text{Ca}(\text{SO}_4)_3$, MgSO_4 , hexagonal CaSO_4 , and orthorhombic CaSO_4 . *Spectrochim Acta A* 55:795–805
- Sun M, Rousse G, Abakumov AM, Saubanère M, Doublet M-L, Rodríguez-Carvajal J, Van Tendeloo G, Tarascon J-M (2015) $\text{Li}_2\text{Cu}_2\text{O}(\text{SO}_4)_2$: a possible electrode for sustainable Li-based batteries showing a 4.7 V redox activity vs Li^+/Li^0 . *Chem Mater* 27:3077–3087
- Vergasova LP, Filatov SK (2012) New mineral species in products of fumarole activity of the Great Tolbachik Fissure Eruption. *J Volcanol Seismol* 6:281–289
- Wildner M (1992) On the geometry of $\text{Co}(\text{II})\text{O}_6$ polyhedra in inorganic compounds. *Z Kristallogr* 202:51–70
- Zelenski M, Malik N, Taran NY (2014) Emissions of trace elements during the 2012–2013 effusive eruption of Tolbachik volcano, Kamchatka: enrichment factors, partition coefficients and aerosol contribution. *J Volcanol Geotherm Res* 285:136–149

Publisher's Note Springer Nature remains neutral with regard to jurisdictional claims in published maps and institutional affiliations.